Giant thermoelectric figure of merit in multivalley high-complexity-factor LaSO

Roberta Farris,[1,*] Francesco Ricci,[2,†] Giulio Casu,[1] Diana Dahliah,[2,‡] Geoffroy Hautier,[2,§] Gian-Marco Rignanese,[2] and Vincenzo Fiorentini[1]

[1]*Dipartimento di Fisica, Università of Cagliari, Cittadella Universitaria, I-09042 Monserrato (CA), Italy*

[2]*Institute of Condensed Matter and Nanosciences (IMCN), Université Catholique de Louvain, Chemin des Étoiles 8, B-1348 Louvain-la-Neuve, Belgium*

(Received 6 October 2021; accepted 2 December 2021; published 17 December 2021)

We report a giant thermoelectric figure of merit ZT (up to six at 1100 K) in n-doped lanthanum oxysulphate LaSO. Thermoelectric coefficients are computed from *ab initio* bands within Bloch-Boltzmann theory in an energy-, chemical potential-, and temperature-dependent relaxation time approximation. The lattice thermal conductivity is estimated from a model employing the *ab initio* phonon and Grüneisen-parameter spectrum. The main source of the large ZT is the significant power factor which correlates with a large band complexity factor. We also suggest a possible n-type dopant for the material based on *ab initio* calculations.

DOI: 10.1103/PhysRevMaterials.5.125406

I. INTRODUCTION

Thermoelectric materials, which convert heat into electricity via the Seebeck effect, have attracted considerable interest as components of power generation devices. In addition to being scalable and reliable, thermoelectric generators are silent and require no moving parts. Sufficiently cheap and efficient thermoelectric devices, therefore, have massive potential for waste-heat recovery in a variety of industrial and consumer processes, such as automotive exhausts, home heating, and large-scale commercial processes [1]. Industrial thermoelectric devices are still comparatively expensive and inefficient and are often relegated to niche applications despite their potential. Nonetheless, this might change in a number of ways; for example, a breakthrough material might be be found with a high conversion efficiency as measured by the figure of merit,

$$ZT = \frac{\sigma S^2}{\kappa_e + \kappa_L} T, \tag{1}$$

where σ is the electrical conductivity, S is the Seebeck coefficient, T is the temperature, and κ_e, κ_L are the electronic and lattice thermal conductivities. It is, thus, only natural that much research is aimed at finding materials with large ZT.

In this framework, the band complexity factor C has emerged as a very relevant parameter from a large-scale data-mining study [2]. Indeed, the power factor $\mathrm{PF} = \sigma S^2$ appearing in the numerator of Eq. (1) exhibits a power-law increase $\mathrm{PF} \sim C^{0.6}$ as a function of C. The latter is actually obtained as $C = N_v K_v$, where N_v is the multiplicity, i.e., the number of equivalent extrema within the Brillouin zone (BZ), and K_v is a measure of the anisotropy of the relevant band extremum (the ratio of geometric and harmonic averages of the diagonal elements of the mass tensor to the power of 3/2). Thus, multiple band-structure extrema (each potentially involving multiple bands) and anisotropic masses are expected to be conducive to large power factors. A quick evaluation readily shows that the most direct power-factor amplifier is the band-valley multiplicity N_v, whereas the K_v factor deviates significantly from 1 (isotropic case) only for energy surfaces with unusually strong anisotropy.

In this paper, we study a material with a large complexity factor (mostly due to a large N_v) from which follow very large PFs and predicted ZT's, despite a not especially favorable lattice thermal conductivity. Lanthanum sulfoxide (LaSO) was identified as a candidate by screening a large (so far, unpublished) database of calculated band extrema. Methodologically, such database searches for significant complexity factors (and especially valley multiplicity) appear to provide useful guidance in the quest for thermoelectric materials.

II. METHODS AND RESULTS

A. General

The ingredients of ZT are the electronic transport coefficients (electrical and electronic-thermal conductivity, Seebeck thermopower) obtained from the electronic structure, and the lattice thermal conductivity, which we discuss specifically in Sec. II C.

The electronic transport coefficients are computed from the *ab initio* density-functional band structure as a function of temperature and doping in the relaxation-time approximation to the linearized Boltzmann transport equation, an approach known as Bloch-Boltzmann theory [3,4]. We use a model of temperature- and energy-dependent relaxation time described at length in previous papers [5,6] as implemented in a publicly

*Present address: ICN2, Barcelona, Spain.

†Present address: Materials Sciences Division, Lawrence Berkeley National Laboratory, Berkeley, CA 94720, USA.

‡Permanent address: Department of Physics, An-Najah National University, Nablus, Palestine.

§Present address: Dartmouth College, Dartmouth, NH 03755, USA.

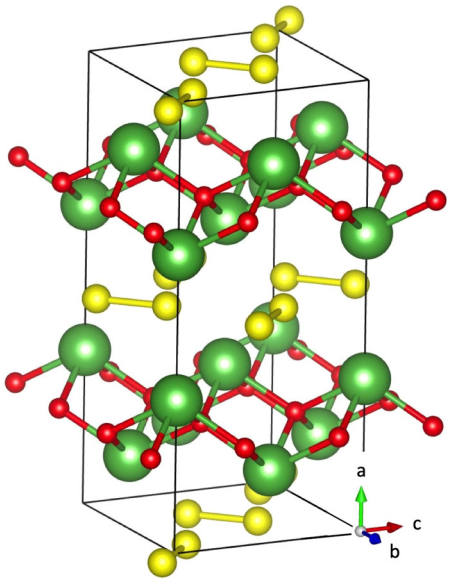

FIG. 1. Sketch of the conventional cell of LaSO (La: large balls; O: small; S: intermediate).

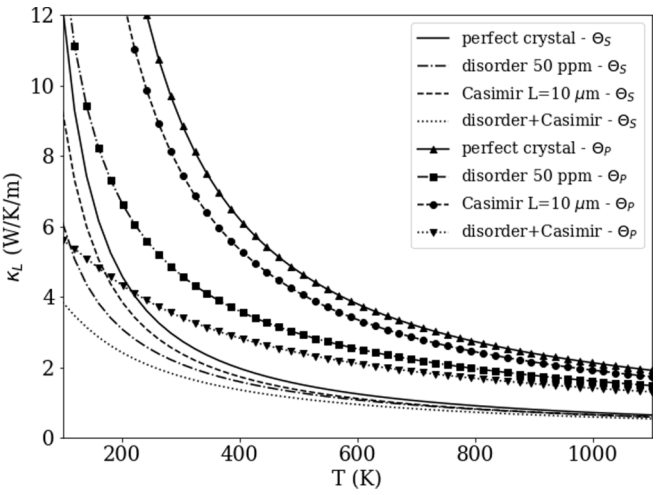

FIG. 2. Lattice thermal conductivity of LaSO for the perfect crystal, for atomic disorder at 50 ppm (10^{18} cm^{-3}), for polycrystalline size 10 μm, and for disorder plus finite size. The two sets of curves correspond to two different definitions [11,13], and, hence, values of the Debye temperature: $\Theta_S = 215$ K (lines) and $\Theta_P = 335$ K (lines with circles).

available custom code [5,7]. We concentrate on *n*-type doping, although *p* doping also gives interesting values.

B. Electronic-structure calculations

Ab initio density-functional structure optimization and band-structure calculations are performed within the generalized-gradient approximation (GGA) using the Perdew-Burke-Ernzerhof functional [8] (hereafter simply labeled as GGA) and the projector augmented-wave method [9] using the VASP code [10] with the La, S, and O_s datasets at the maximum suggested cutoff. LaSO has an orthorhombic structure (Fig. 1) with space-group *Cmca*. It is optimized following quantum forces and stress in a conventional cell containing eight formula units. The material is made of strongly buckled La-O bonded planes intercalated in the *a* direction by molecular-crystal-like layers of S dimers. The resulting computed lattice constants are $a = 13.323$, $b = 5.950$, and $c = 5.945$ Å. As expected, transport is found to be less efficient in the *a* direction than on the *bc* plane. The electronic states are calculated on a $(12 \times 24 \times 24)$ *k*-point grid. The minimum gap in GGA is 1.3 eV, so the *n*-type thermoelectric coefficients are essentially unaffected by valence states (we checked this using a scissor operator which adjusts the gap to the value obtained by hybrid functional calculations, see Sec. II G). The band structure will be discussed further in Sec. II E.

C. Lattice thermal conductivity

We estimate the lattice thermal conductivity κ_L using the model of Ref. [11]. In the present subsection, the equation numbers refer to that paper. We compute the phonon spectrum and Grüneisen parameters from first principles using density-functional perturbation theory with the QUANTUM ESPRESSO [12] code using ultrasoft pseudopotentials and GGA. The phonon-phonon relaxation time is computed from Eqs. (3) and (7), where for the parameter γ, we use the Grüneisen density of states obtained from the calculated spectrum, instead of the average Grüneisen value (which we can calculate and find to be 0.78). Beside phonon-phonon scattering, Casimir and disorder scattering can be easily introduced via Eqs. (21) and (22) (assuming, for example, that disorder originates from O vacancies). The sound velocity is approximated à la Debye (constant below the Debye energy $k_B\Theta$, zero above); its value is the harmonic average $s = 3134$ m/s of the computed small-wave vector acoustic-branch velocities. The thermal conductivity is finally obtained from Eq. (2) with energy dependence only.

Figure 2 shows the lattice thermal conductivity for two Debye temperatures, $\Theta_S = 215$ K as obtained from our data according to the definition of Eq. (10), and $\Theta_P = 335$ K with the definition by Pässler [13]. The choice of Θ changes considerably the conductivity because the phonon-phonon scattering time depends exponentially on Θ. In the following we will compare results obtained with κ_L for the perfect crystal with these two Debye tempeatures (the higher curves for each of the two Θ's). Figure 2 also shows κ_L for a few combinations of size and disorder parameters; weak disorder or micron-sized-crystalline Casimir scattering clearly have comparatively minor effects on the scale set by the choice of Θ, so we will not expound upon them further.

Discussion

The accuracy of the estimate of ZT to be discussed below clearly depends on the lattice conductivity as a hypothetically much larger κ_L would directly reduce ZT. A full *ab initio* computation [6] is costly and impractical for this material, hence, out of our present scope. Nevertheless, we reckon that the model calculation of κ_L should be sufficient for the present purposes: It has the correct asymptotic behavior; it includes the density of states and specific heat obtained *ab initio*, as

well as the *ab initio* Grüneisen parameters in the relaxation time; the only model part is the relaxation time whereby, in particular, the key parameter is, as mentioned, Θ for which we use two different possible definitions; finally, the model appears to err on the side of giving too large a κ_L [11] compared to experiments and other techniques.

Adding to this the fact that we use the worst possible κ_L (that for the crystal) to calculate ZT below, whereas in a real material κ_L will be smaller (e.g., defected, doped, polycrystalline, etc.), we ultimately expect no significant ZT reductions compared to our estimates (rather, even an increase). This is because the defining feature of this material is, in fact, the large electronic power factor.

D. Transport coefficients and electronic relaxation time

We compute the transport coefficients with a code [5,7] employing parts of the BOLTZTRAP2 [4] transport code as libraries and including energy- and temperature-dependent relaxation time. The *ab initio* bands (assumed rigid, i.e., not changing with doping or temperature) are interpolated by a Fourier-Wannier technique [4] over a k-point grid with 64 times more points than the *ab initio* one, i.e., approximately equivalent to a $(48 \times 96 \times 96)$ grid.

As discussed, for instance, in Ref. [6], a constant relaxation time $\tau = \tau_0$ neglects relevant physics in the electron scattering (thermal distributions, local masses, energies of phonons, and more). So we adopt a temperature- and energy-dependent relaxation time $\tau(T, E, \mu) = 1/P_{\text{imp}} + 1/P_{\text{ac}} + 1/P_{\text{polar}}$ which enters the kernel σ of the integral in Eq. (9) of Ref. [4] (additional details can be found in Ref. [5]). The P's are the scattering rates of charged impurities, acoustic phonons, and polar optical phonons given in Refs. [6,14,15]. Piezoelectric scattering is zero by symmetry [14,16]. We point out that there is no effective mass approximation in the transport coefficient calculations, except those implicit in the relaxation time.

The parameters entering the model for τ can be computed directly. The conduction-band deformation potential is $D = 2.1$ eV, the density is 5270 kg m^{-3}, and the effective conduction mass is set to a conservatively large $m_c^* = 0.5 m_e$. The phonon energies, dielectric tensor, and sound velocity are obtained from linear-response calculations [12] as in Sec. II C. The sound velocity is 3134 m/s as discussed in the previous section. For the dielectric constants, we use the harmonic averages of the (very similar) b and c components, $\varepsilon_\infty = 6.23$, and $\varepsilon_{\text{static}} = 18.73$ (as it turns out, the a direction is quite irrelevant for thermoelectricity).

A key point is the scattering by polar (i.e., optical) phonons, which dominates the total scattering rate. The longitudinal optical (LO) phonon energies are calculated directly using the linear-response approach (Sec. II C) with nonanaliticity along the crystallographic directions. Since LO phonons scatter electrons with momentum parallel to the LO polarization vector, a direction-dependent polar-phonon τ would be needed. To simplify the procedure, we use a set of effective LO energies (20, 27, and 30 meV) obtained as averages of the three LO groups of frequencies over the a, b, and c directions. We deem this simplification to be quite acceptable in view of the other significant uncertainties in the calculations, such as the choice of Θ in the lattice thermal conductivity, or our choice of using a single-phonon replica in the polar-phonon scattering rate.

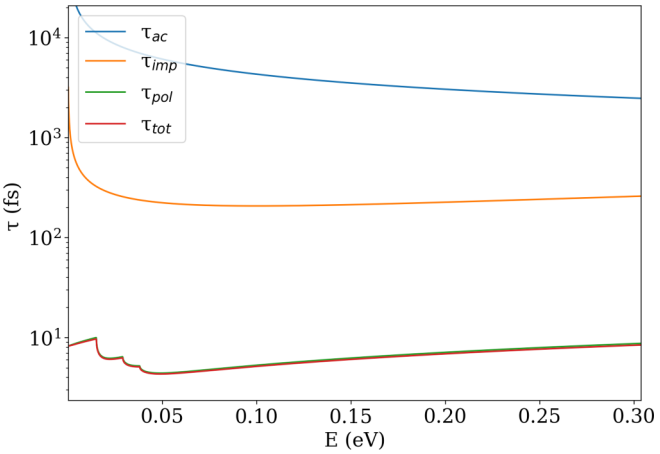

FIG. 3. Relaxation time vs E for $T = 600$ K and $\mu = 0$ for the b axis. From the top: acoustic-phonon, impurity, polar-phonon, and total.

The relaxation time $\tau(E, T)$ is sketched vs E in Fig. 3. As typical of polar insulators, the polar-phonon scattering dominates, and its downward jump across the LO phonon energies is in the low-energy region relevant for transport. Here, we use this relaxation time accounting self-consistently for chemical potential changes and do not employ any average-time or constant-time approximations.

E. Band structure and complexity factors

We now discuss the band structure of LaSO and two versions of the complexity factor. The first, C_b is a geometrical value derived from the number of valleys and the masses from the band structure. The second, C_t is a transport value obtained *a posteriori* from the calculated transport properties with the procedure of Ref. [2]. The data are summarized in Fig. 4, reporting the conduction-band Fermi surface of n-doped LaSO at several chemical potentials, and Fig. 5, displaying the bands, the carrier density (the conduction density of states multiplied by the Fermi distribution), and the complexity factor C_t.

The low-energy valleys of the LaSO conduction band occur at four internal points of the BZ and at four zone-border points (which count as two internal points). By inspection, the first four conduction states (marked in different colors in Fig. 4) provide 16 available valleys within about 150 meV of the band edge. These are visible in the Fermi surface in Fig. 4. Four valleys provided by the first band are internal to the BZ. Eight valleys, from the second band, are located on the square faces and, therefore, shared with adjacent BZs (hence, their weight is 1/2). Eight valleys come from the third band (specifically on the segments Z-Z_1 and S-Y/S-Y_1, Fig. 5), and eight more from the fourth band on the same segment.

The same result is found by counting the relevant bands in Fig. 5. The stationary point on the P-U segment and its three symmetry partners contribute a total of eight bands; points S and Z with their two symmetry partners contribute two

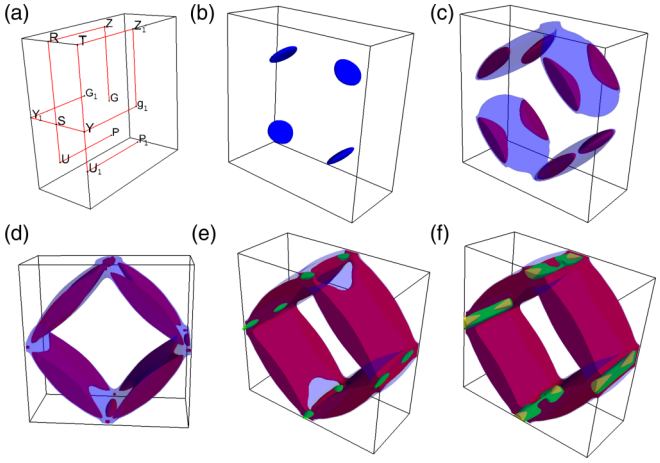

FIG. 4. (a) Brillouin zone with the high-symmetry points path used in Fig. 5. Other panels: Fermi surface at (b) 0.01 eV, (c) 0.07 eV, (d) 0.1 eV, (e) 0.11 eV, and (f) 0.13 eV above the conduction edge. The conduction bands involved are colored in blue (first band), red (second band), green (third band), and yellow (fourth band).

bands each (accounting for their being at the zone border); that amounts again to 16 available band minima.

The carrier density vs energy (in the central panel of Fig. 5) shows that all these bands are occupied at the chemical potentials and temperatures of interest (i.e., μ near the lowest conduction edge, and temperatures on the order of one to three times room temperature). Accordingly, all the bands just mentioned may be considered active (i.e., contributing to the transport) so that the effective total multiplicity of the occupied valleys is $N_v = 16$. From Fig. 5, we can also infer that the optimal doping level, namely, the doping at which ZT is maximal for a given T, will probably fall in the low 10^{20} cm^{-3}, and that the Seebeck coefficient may be interesting due to the fast rise of the density of states near the band edge.

As it turns out, the relevant directions for conduction are on the basal *b*-*c* plane of the material. The masses in the in-plane directions are quite isotropic, so $K_v \simeq 1$, and the geometrical complexity factor is $C_b \simeq 16$. If the *a* component of the mass tensor was to be considered, a larger anisotropy would arise, resulting in $K \simeq 1.2$–1.3, i.e., a C_b of about 20. (The anisotropy can be appreciated, for example, from the different curvatures of the bands at point S, respectively, along the Y-S-Y$_1$ segment and along the U-S-R segment).

The transport complexity factor C_t is in the rightmost panel of Fig. 5. It is computed from the calculated transport coefficients on the basal plane as outlined in Ref. [2] using a constant relaxation-time $\tau_0 = 10$ fs, purely for consistency with Ref. [2]. We set the scattering parameter $\lambda = 1$ in the Seebeck coefficient model of Ref. [2] to take into account the dominant polar scattering we have in the present case. Similar to most quantities in thermoelectricity, C_t is a temperature- and chemical potential-dependent tensor. To compare it with the geometric C_b (a scalar), we pick a low $T = 300$ K and $\mu = 0$ and average over in-plane directions. C_t at 300 K is relatively flat at low energy, and its energy average is roughly 15, in quite decent agreement with $C_b = 16$ obtained above. This is in line with our having considered just the in-plane largely isotropic transport. We discuss in Sec. II F (especially with reference to Figs. 6 and 7) the connection of our C values with the rule of thumb of Ref. [2].

F. Thermoelectric coefficients and figure of merit

Figure 6 reports the Seebeck coefficient, the electrical conductivity, the electronic thermal conductivity, and the power factor vs doping and parametrized by T. Figure 7 displays the same quantities vs T at optimal doping (i.e., the doping at which ZT is a maximum at the given temperature). For simplicity, only the *b* component is plotted in Fig. 6. As seen in Fig. 7, the *c* and *b* components are very close, and the *a* component ends up producing a small power factor and ZT, so it can be ignored.

The large conductivity and Seebeck coefficient result in a large power factor for the in-plane transport with a maximum of 15 mW/(K^2 m) at 400 K. We can now make contact between the large complexity factors $C_t \sim C_b \simeq 16$ discussed in the previous section and the rule of thumb of Gibbs *et al.* [2]. For this complexity factor, Fig. 3 of Ref. [2] suggests that the expected maximum power factor should be between 6 and 22 mW/(K^2 m). Using the setting of Ref. [2] ($\tau = \tau_0 = 10$ fs and $T = 600$ K), we indeed obtain a power factor of 21 mW/(K^2 m). With the full relaxation-time treatment, the power factor at 600 K (Fig. 7) is about 12 mW/(K^2 m). In both cases, our results are consistent with the general prediction [2].

Finally, in Fig. 8, we show the ZT tensor for the two instances of lattice thermal conductivity discussed in Sec. II C. The left panels report the diagonal components of ZT as a function of T at optimal doping, and the right panels report the *b* component as a function of doping for different temperatures. The *b* and *c* components differ by only a fraction of a percent. The main results in this figure are as follows: (i) ZT is very large, reaching values well over 3 and, respectively, 6 at high T for the two versions of the lattice thermal conductivity; *(ii)* the optimal doping is in the low to mid-10^{20} cm^{-3}, depending on κ_L and T. ZT may still be rather interesting even at lower doping: for example, it is already above 2 at 800 K and 2×10^{19} cm^{-3} (Fig. 8, upper panel). We recall again that all coefficients refer to electrons in perfect-crystal bands, subject to scattering from phonons and charged impurities so that no scattering is accounted for from disorder, dislocations, neutral impurities, extended defects, etc. which could affect transport in ways we cannot quantify.

G. Doping

Given the relatively high carrier density required to obtain interesting ZT's, we now look into the possibility of *n*-type doping of LaSO. Screening a number of options, we find that Hf seems to be a reasonable candidate donor.

Dopability is difficult to assess in any material, and LaSO is no exception. In particular, here we do not address possible compensation by native defects or other contaminants, but only the solubility and ionization of donors. Also, our discussion is based on equilibrium thermodynamics, so the possibility remains that epitaxial growth (which often occurs out of equilibrium), ion implantation, and certain

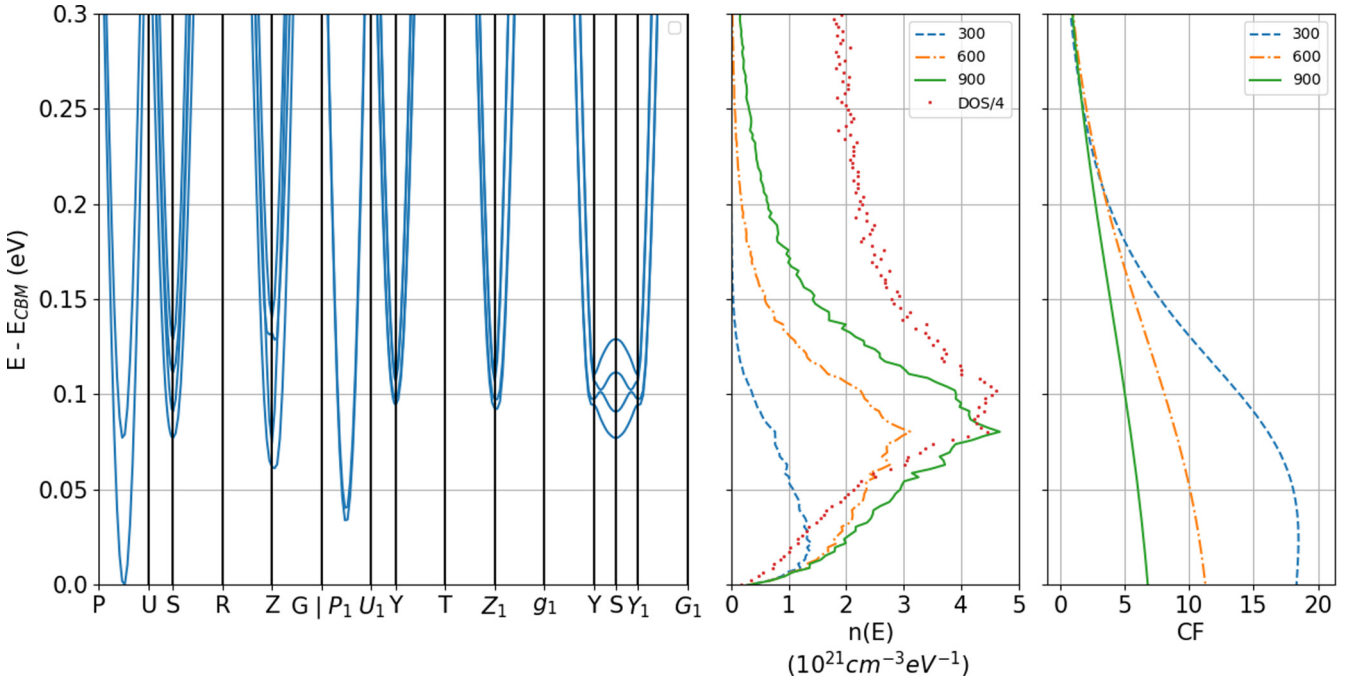

FIG. 5. Left: conduction bands of LaSO along the paths marked in Fig. 4(a). Center: the density of states and carrier density (i.e., the conduction density of states multiplied by the Fermi distribution) both in units of 10^{21} cm^{-3} eV^{-1} vs energy. Right: complexity factor for the b direction (c is similar, a is about zero) vs energy. The zero of energy is the conduction minimum. In the center and right panels, $\mu = 0$ and $T = 300$, 600, and 900 K.

kinds of diffusion doping processes may do better than we predict here.

Solubility and carrier concentrations are estimated from the formation energies and thermal ionization levels obtained via *ab initio* calculation. We use VASP, on 144-atom supercells with a $4 \times 4 \times 4$ k-point grid and the GGA, the details being the same as in the calculations in the previous sections. For charged states, we use the simple monopole correction by Leslie and Gillan [17] with the dielectric constant calculated in Sec. II D.

We concentrate on potential donors substituting on the La site (namely, Zr, Hf, Ce, Sb, Bi, Sn, and Si) as we find that potential substitutions for O or S, such as F or Cl, tend to go interstitial or have large formation energy. Si can be discarded offhand because of its huge formation energy. Sb, Bi, and Sn can be neglected as well since they have no state (in particular, no donor state) in the vicinity of the gap. This effective trivalent behavior is presumably due to the hybridization cost of the s orbital, and the pyramidal bonding geometry of the La site which does not favor sp hybrids. For the remaining dopants Zr, Hf, and Ce, we find the thermal levels reported in

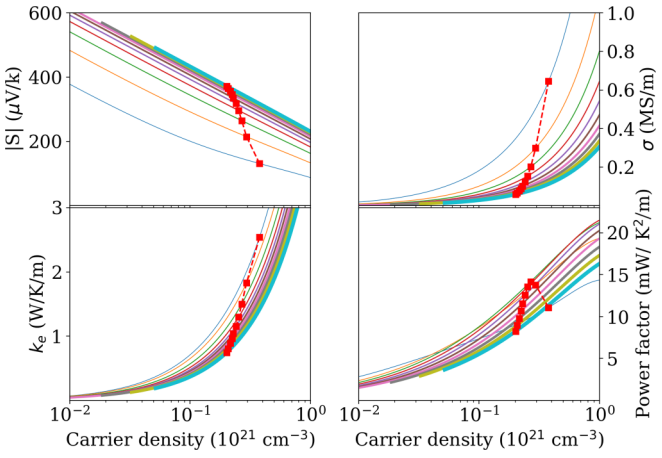

FIG. 6. Seebeck coefficient, conductivity, electronic thermal conductivity, and power factor vs doping at T increasing from 200 to 1100 K, denoted by increasing line thickness. The red squares are values at optimal doping.

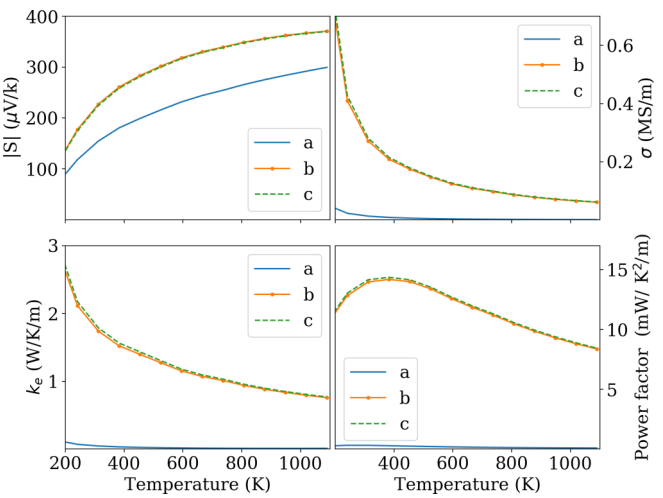

FIG. 7. Seebeck coefficient, conductivity, electronic thermal conductivity, and power factor vs T at optimal doping.

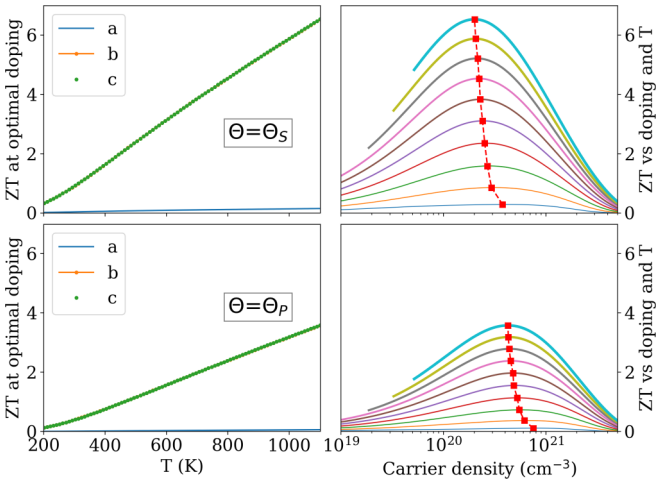

FIG. 8. ZT of LaSO. Left panels: ZT vs T at optimal doping; right panels: ZT vs doping (b component only) and various T's. Top panels: lattice thermal conductivity calculated with $\Theta = \Theta_S$; bottom panels: the same for $\Theta = \Theta_P$. Temperatures 200 to 1100 K, line thickness proportional to T. All quantities are drawn on identical scales for easier comparison. Note that on this scale the a component is very small, and the b and c components are practically indistinguishable.

Table I. Neutral Ce has an electron in a f orbital when substituting for trivalent La, and its donor level is deep in GGA. This will not improve when using non-local-density methods (such as hybrid functionals) which remove self-interaction and tend to lower the energy of very localized occupied states. Luckily, instead, Zr and Hf have shallow thermal levels lying just above the conduction edge in GGA (although there are, as usual, large uncertainties in these estimates at the very least ±0.1–0.2 eV). A python notebook with the formation energies and their postprocessing is in Ref. [18]. To check for the effects of more advanced exchange-correlation functionals, we calculated the thermal level for Zr using the hybrid HSE functional [19] and found a value similar to the GGA. This is further confirmed by the electronic band structure, which exhibits impurity-related resonant states within the lower portion of the conduction band at the same position both in the GGA and the HSE. In passing, the gaps are 1.3 eV in the GGA and 2.9 eV in the HSE, the difference being within 15% of that predicted by the dielectric correction rule [20].

Another interesting result of these calculations is that the upper valence band and the bottom conduction band are predominantly sulfurlike so that conduction effectively occurs in-plane in the S layers. Carriers living in the S layer may, thus, be partially decoupled from charged impurities in the La-O layers, leading to a reduced impurity scattering.

To present synthetically the results as a function of an operational quantity, we report in Fig. 9 the density of carriers

TABLE I. Donor thermal levels (eV from the conduction edge).

Dopant	Hf	Zr	Zr Heyd-Scuseria-Ernzerhof (HSE)	Ce
ε	+0.05	+0.05	+0.07	–0.56

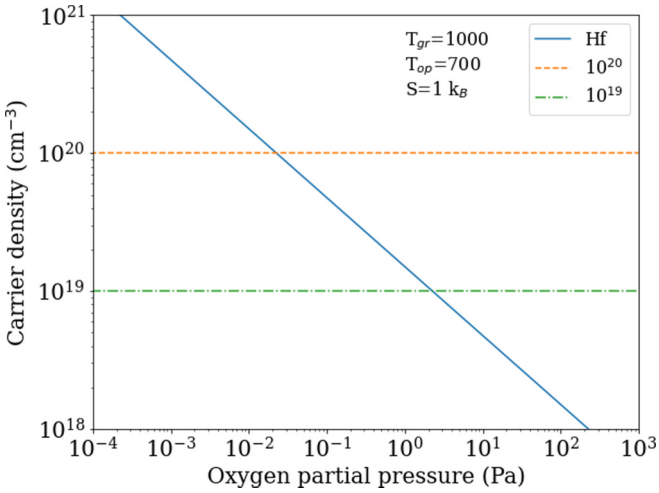

FIG. 9. Carrier density vs oxygen partial pressure for Hf doping (see the text for details).

vs the oxygen partial pressure at a typical device operating temperature $T_{\rm op} = 700$ K and with Hf incorporated in LaSO in thermal equilibrium during growth at temperature $T_{\rm gr}$. The rationale for this is that, as we now discuss in more detail, the partial pressure is related to the formation energy of the donor via the oxygen chemical potential, hence, determines the doping level.

More specifically, the carrier density N_c at $T_{\rm op}$ is computed as

$$N_c = N_d \exp\left(-\eta/k_B T_{\rm op}\right), \tag{2}$$

originating from a dopant thermal level at energy η below to the conduction edge with a dopant density

$$N_d = N_s \exp\left(-E_{\rm f}/k_B T_{\rm gr} + S\right) \tag{3}$$

embedded in thermodynamical equilibrium at the growth temperature $T_{\rm gr}$ (we assume $T_{\rm gr} = 1000$ K). The vibrational formation entropy is arbitrarily but conservatively set to $S = 1k_B$, and there are $N_s = 1.697 \times 10^{22}$ cm^{-3} available sites. For a normal dopant having a level below the band edge, $\eta = -\varepsilon$ (Table I); but since the Hf level is above the conduction edge, i.e., ε is positive, the ionization Arrhenius factor in Eq. (2) is simply set to 1.

The formation energy is related to the oxygen chemical potential, hence, to the oxygen partial pressure. The dominant solubility limit for Zr and Hf is the formation of dioxides. Since La forms a sesquioxide, the Hf substitution causes an excess of oxygen. Therefore, the formation energy E_f increases with the oxygen chemical potential, and it is at its largest in oxygen-rich conditions, namely,

$$E_f = C + \frac{(\mu_{\rm O} - \mu_{\rm O_2})}{2}, \tag{4}$$

with $\mu_{\rm O} \leqslant \mu_{\rm O_2}$ and

$$C = E_{\rm def} - E_{\rm bulk} + \mu_{\rm La_{bulk}} - \mu_{\rm Hf_{bulk}} - \Delta H_{\rm HfO_2} + \Delta H_{\rm La_2O_3},$$

where $E_{\rm def}$ and $E_{\rm bulk}$ are the defected and pristine supercell energies, the μ's are the chemical potentials of the bulk elements, $\mu_{\rm O_2}$ is the chemical potential of O in an O_2 molecule, and ΔH is the oxide formation enthalpies. $E_{\rm def}$ and $E_{\rm bulk}$

are calculated directly, the bulk chemical potentials are taken from experiment, and formation enthalpies are from the Materials Project [21]. Finally, the O partial pressure at growth temperature T_{gr} is related to the oxygen chemical potential μ_O by the standard relation $p = p_0 \exp[(\mu_O - \mu_{O_2})/k_B T_{gr}]$ and $p_0 = 19$ kPa the normal-conditions oxygen partial pressure.

The dopant density increases as the chemical potential goes more and more negative, i.e., the partial pressure is reduced, and this offers some leeway to increase the density by adopting O-lean growth conditions. As Fig. 9 shows, Hf can, indeed, produce useful carrier densities in the 10^{20}-cm^{-3} range for low but not unreasonable O partial pressures. Since the O vacancy is most likely a deep donor as it is in most oxides, oxygen deficiency should not cause notable counterdoping. Zr, in turn, is unfortunately ruled out by its comparatively larger formation energy.

III. SUMMARY

We predicted a giant thermoelectric figure of merit in high-valley-multiplicity lanthanum oxysulphate LaSO. The GGA *ab initio* band structure, interpolated over a fine grid, is fed into Bloch-Boltzmann theory, accounting for an energy- and temperature-dependent relaxation time [4] (code available in Ref. [7]). The lattice thermal conductivity is obtained from a model using the *ab initio* phonon dispersion, Grüneisen parameters, and the Debye temperature. For the perfect crystal, ZT is practically linear in T and at 1100 K reaches a value between 3.5 and 6.5 depending on the lattice thermal conductivity. The optimal doping is weakly temperature dependent and in the low- to mid-10^{20}-cm^{-3} range. Our results for the power factor confirm earlier suggestions [2] that high valley multiplicity leads to large power factors and, therefore, large ZT. The n-type dopability of LaSO was also analyzed, suggesting Hf as a potential dopant.

ACKNOWLEDGMENTS

F.R. and G.-M.R. acknowledge support from the "Low Cost ThermoElectric Devices" (LOCOTED) Project funded by the Région Wallonne (Programmes FEDER) and from CISM and CECI for computational support. V.F., R.F., and G.C. thank CINECA for ISCRA supercomputing grants. R.F. thanks ICMN-UCL for hospitality. V.F. is on secondment leave at the Italian Embassy to Germany; his views as expressed herein are not necessarily shared by the Italian Ministry of Foreign Affairs.

[1] T. M. Tritt and M. A. Subramanian, MRS Bull. **31**, 188 (2006).
[2] Z. M. Gibbs, F. Ricci, G. Li, H. Zhu, K. Persson, G. Ceder, G. Hautier, A. Jain, and G. J. Snyder, npj Comput. Mater. **3**, 8 (2017).
[3] P. B. Allen, Phys. Rev. B **17**, 3725 (1978); P. B. Allen, W. E. Pickett, and H. Krakauer, *ibid.* **37**, 7482 (1988).
[4] G. K. H. Madsen, J. Carrete, and M. J. Verstraete, Comput. Phys. Commun. **231**, 140 (2018).
[5] G. Casu, A. Bosin, and V. Fiorentini, Phys. Rev. Mater. **4**, 075404 (2020).
[6] R. Farris, M. B. Maccioni, A. Filippetti, and V. Fiorentini, J. Phys.: Condens. Matter **31**, 065702 (2019); M. B. Maccioni, R. Farris, and V. Fiorentini, Phys. Rev. B **98**, 220301(R) (2018).
[7] Available on Gitlab at http://tiny.cc/houqkz.
[8] J. P. Perdew, K. Burke, and M. Ernzerhof, Phys. Rev. Lett. **77**, 3865 (1996).
[9] P. E. Blöchl, Phys. Rev. B **50**, 17953 (1994); G. Kresse and D. Joubert, *ibid.* **59**, 1758 (1999).
[10] G. Kresse and J. Furthmüller, Phys. Rev. B **54**, 11169 (1996).
[11] L. Bjerg, B. B. Iversen, and G. K. H. Madsen, Phys. Rev. B **89**, 024304 (2014).
[12] P. Giannozzi *et al.*, J. Phys.: Condens. Matter **21**, 395502 (2009); **29**, 465901 (2017).
[13] R. Pässler, J. Appl. Phys. **101**, 093513 (2007).
[14] B. K. Ridley, J. Phys.: Condens. Matter **10**, 6717 (1998).
[15] B. K. Ridley, *Quantum Processes in Semiconductors* (Clarendon, Oxford, 1988).
[16] M. I. Aroyo, J. M. Perez-Mato, D. Orobengoa, E. Tasci, G. de la Flor, and A. Kirov, Bulg. Chem. Commun. **43**, 183 (2011); J. M. Perez-Mato, S. V. Gallego, E. S. Tasci, L. Elcoro, G. de la Flor, and M. I. Aroyo, Annu. Rev. Mater. Res. **45**, 217 (2015); Bilbao crystallographic server: http://www.cryst.ehu.es
[17] M. Leslie and M. J. Gillan, J. Phys. C: Solid State Phys. **18**, 973 (1985).
[18] https://gitlab.com/vfiore/laso-eform.
[19] J. Heyd, G. E. Scuseria, and M. Ernzerhof, J. Chem. Phys. **118**, 8207 (2003).
[20] V. Fiorentini and A. Baldereschi, Phys. Rev. B **51**, 17196 (1995).
[21] A. Jain, S. P. Ong, G. Hautier, W. Chen, W. D. Richards, S. Dacek, S. Cholia, D. Gunter, D. Skinner, G. Ceder, and K. A. Persson, APL Mater. **1**, 011002 (2013).